Conf-940142--48

LA-UR- 94-378

Title: TIME-DEPENDENT NUMERICAL SIMULATION OF VERTICAL CAVITY LASERS

Author(s): L. E. Thode, G. Csanak, L. L. So, T. J. Kwan, M. Campbell, and M. Tan

Submitted to: OE/LASE '94
Los Angeles, CA
January 22-29, 1994

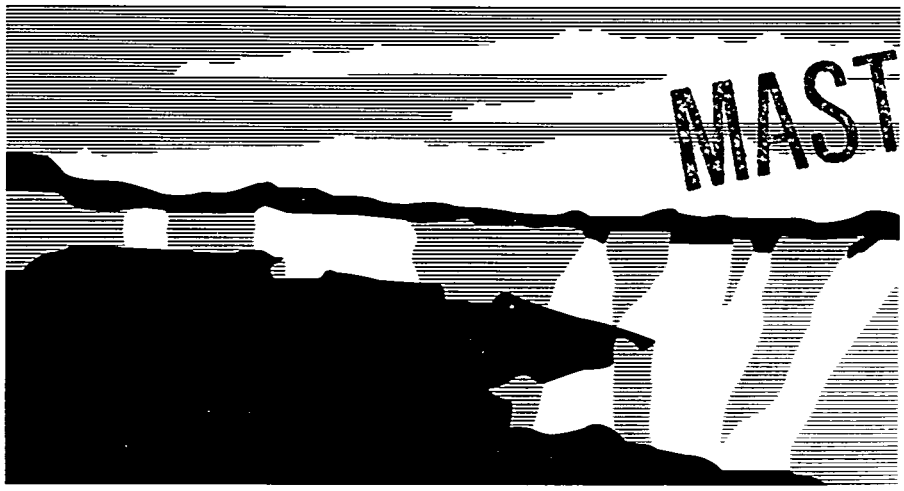

Los Alamos
NATIONAL LABORATORY

Form No. 836 R5
ST 2629 10/91

DISCLAIMER

Portions of this document may be illegible in electronic image products. Images are produced from the best available original document.

Time-dependent numerical simulation of vertical cavity lasers

L. E. Thode, G. Csanak, L. L. So, and T. J. T. Kwan
Los Alamos National Laboratory, Los Alamos, NM 87544
M. Campbell
PASTDCO, Albuquerque, NM 87106

ABSTRACT

To simulate vertical cavity surface emitting lasers (VCSELs), we are developing a three-dimensional, time-dependent field-gain model with absorption in bulk dielectric regions and gain in quantum well regions. Since the laser linewidth is narrow, the bulk absorption coefficient is assumed to be independent of frequency with a value determined by the material and the lattice temperature. In contrast, the frequency-dependent gain regions must be solved consistently in the time domain. Treatment of frequency-dependent media in a finite-difference time-domain code is computationally intensive. However, because the volume of the quantum well regions is small relative to the volume of the multilayer dielectric (MLD) mirror regions, the computational overhead is reasonable. A key issue is the calculation of the fields in the MLD mirror regions. Although computationally intensive, good agreement has been obtained between simulation results and matrix equation solutions for the reflection coefficient, transmission coefficient, and bandwidth of MLD mirrors. We discuss the development and testing of the two-dimensional field-gain model. This field-gain model will be integrated with a carrier tranport model to form the self-consistent laser code, VCSEL.

1. INTRODUCTION

In order to understand and optimize quantum well lasers (QWLs) one has to understand and properly describe the dynamical behavior of the device. At a fundamental level there is a need to understand the transverse mode pattern since the output of the QWL will be coupled to an optical fiber. Another important characteristic of the dynamical behavior of the QWL is its modulation bandwidth, which is commonly identified with the frequency of relaxation oscillation.[1,2,3] Simple theories predicted a factor of 3-to-4 improvement in modulation bandwidth for QWLs[4,5] with an additional factor of 2-to-3 improvement for strained QWLs. Unfortunately, these predictions have not been realized in actual devices.[6] To understand these two issues, as well as other discrepancies between theory and experiment, it is necessary to develop a fairly complete QWL model that attempts to take into account all important physical effects. To achieve this goal we have undertaken the development of an a priori model that consists of three coupled systems: Maxwell's equations, the optical Bloch equations (OBEs), and the carrier transport equations. Using this a priori model as a benchmark for the calculation of the transverse modes, a reduced model will be developed to provide a more computationally efficient approach toward VCSEL design.

2. FIELD MODEL

In MKS units, Maxwell's equations are

$$\frac{\partial \mathbf{B}}{\partial t} = -\nabla \times \mathbf{E} \tag{1}$$

and

$$\frac{\partial \mathbf{D}}{\partial t} = \nabla \times \mathbf{B} - \mathbf{J}, \tag{2}$$

where $\mathbf{J}$ is the conduction current density. To obtain a set of field equations for the VCSEL, we make three basic assumptions concerning Ampère's law, Eq. 2. First, the material is nonmagnetic. In that case, the magnetic induction, $\mathbf{B}$, is related to the magnetic field, $\mathbf{H}$, by the vacuum constitutive relation

$$\mathbf{B} = \mu_0 \mathbf{H}. \tag{3}$$

Second, we split the electric displacement, $\mathbf{D}$, into two parts. The first part is the contribution from the real part of the bulk index of refraction, n, while the second part is the polarization, $\mathbf{P}$, associated with the quantum well gain,

$$\mathbf{D} = \varepsilon_0 n^2 \mathbf{E} - \mathbf{P}. \tag{4}$$

THODE

Third, the frequency-independent bulk absorption is described by the simple Ohm's law

$$\mathbf{J} = \sigma\mathbf{E} = \frac{c\alpha}{n}(\varepsilon_0 n^2 \mathbf{E}), \tag{5}$$

where σ and α are the spatially dependent conductivity and absorption coefficient, respectively. At this point, we redefine the electric displacement as

$$\mathbf{D} \equiv \varepsilon_0 n^2 \mathbf{E}, \tag{6}$$

and use Eqs. 3 through 6 to rewrite Ampère's law in the form

$$\frac{\partial \mathbf{D}}{\partial t} = \nabla \times \frac{\mathbf{B}}{\mu_0} - \frac{c\alpha}{n}\mathbf{D} + \frac{\partial \mathbf{P}}{\partial t}. \tag{7}$$

It is convenient to express Eqs. 1 and 7 in dimensionless form. We define $\omega_p = (n_p q^2/\varepsilon_0 m)^{1/2}$ as the plasma frequency and c/ω_p as the scale length for the problem of interest, where q is the electron charge and m is the electron rest mass. Space and time variables are now used in units of c/ω_p and ω_p, respectively. The remaining dimensionless variables are in terms of dimensionless space and time variables and fundamental constants. One is free to choose the scale length. For the VCSEL a reasonable scale length is a micron, $c/\omega_p = 1\mu m$.

In terms of the dimensionless variables, denoted by a tilde, Maxwell's equations for the VCSEL become

$$\frac{\partial \tilde{\mathbf{B}}}{\partial \tilde{t}} = -\tilde{\nabla} \times \tilde{\mathbf{E}} \tag{8}$$

and

$$\frac{\partial \tilde{\mathbf{D}}}{\partial \tilde{t}} = \tilde{\nabla} \times \tilde{\mathbf{B}} - \tilde{\alpha}\tilde{\mathbf{D}} + \frac{\partial \tilde{\mathbf{P}}}{\partial \tilde{t}}. \tag{9}$$

For an orthogonal curvilinear coordinate system, Eqs. 8 and 9 can be rewritten as

$$\frac{\partial (h_j h_k \tilde{B}_i)}{\partial \tilde{t}} = \frac{\partial (h_j \tilde{E}_j)}{\partial \tilde{x}_k} - \frac{\partial (h_k \tilde{E}_k)}{\partial \tilde{x}_j} \tag{10}$$

and

$$\frac{\partial (h_j h_k \tilde{D}_i)}{\partial \tilde{t}} = -\frac{\partial (h_j \tilde{B}_j)}{\partial \tilde{x}_k} + \frac{\partial (h_k \tilde{B}_k)}{\partial \tilde{x}_j} - \tilde{\alpha}(h_j h_k \tilde{D}_i) + \frac{\partial (h_j h_k \tilde{P}_i)}{\partial \tilde{t}}, \tag{11}$$

where

$$h_i{}^2 = \left(\frac{\partial \tilde{x}}{\partial x_i}\right)^2 + \left(\frac{\partial \tilde{y}}{\partial x_i}\right)^2 + \left(\frac{\partial \tilde{z}}{\partial x_i}\right)^2, i = 1,2,3.$$

In this form, the equations are solved on a uniform mesh in the transformed x_i space. In the transformed space there is uniform zoning along each coordinate direction, although the zone sizes can be different in all three directions. The fields are located on the transformed mesh using the Yee alogrithm.[7]

For the VCSEL, the basic coordinate system is taken to be cylindrical, with nonuniform zoning allowed along the longitudinal coordinate, z, and the radial coordinate, r. Furthermore, the solutions are assumed to be periodic along the azimuthal direction: *i. e.*, we assume that for any field component F_i,

$$F_i(z,r,\theta) = \sum_l^{l_{max}} F_i^l(z,r)\exp(il\theta).$$

With this assumption, in Eqs. 10 and 11, the spatial derivative along the azimuthal direction is replaced by

$$\frac{\partial (h_i \tilde{F}_i^l)}{\partial \tilde{x}_3} = l h_i \tilde{F}_i^l.$$

This mode-decomposition of Maxwell's equations in the azimuthal direction was first implemented in the IVORY code with a conduction current source rather than a polarization current source.[8]

THODE

3. GAIN MEDIUM MODEL

The fundamental theory of semi-conductor lasers was developed by Haug, Koch, Sargent, and co-workers. The most complete formulation is due to Haug, [9] who used the Schwinger-Keldysh [10,11] non-equilibrium Green's function technique along with the screened Hartree-Fock approximation for the Coulomb interactions for the description of the interaction of a strong electromagnetic field with a semi-conductor described as a two-component plasma. Haug obtained the Optical Bloch Equations (OBEs) for the electron and hole densities and their coherence. A simple derivation of the same equations was obtained by Lindberg and Koch [12] via a quantum-mechanical projection operator technique. The OBEs obtained by the above investigators were used by Sargent *et al.* [13] to investigate multi-wave mixing in a semi-conductor laser media. They introduced a further approximation by ignoring certain Coulomb interaction terms in the equation for the electron-hole coherence which was permitted in the gain regime.

Following Sargent *et al.* we write the fundamental equations for a semi-conductor laser in the form

$$\frac{\partial \rho_{cv}}{\partial t} = -(i\omega + \gamma)\rho_{cv} + iV_{cv}(N_e + N_h - 1) \tag{12}$$

$$\frac{\partial N_e}{\partial t} = \lambda_e - \gamma_{nr} N_e - \Gamma N_e N_h - \left.\frac{\partial N_e}{\partial t}\right|_{c-c} - (iV_{cv}\rho_{vc} - iV_{cv}^*\rho_{cv}) \tag{13}$$

$$\frac{\partial N_h}{\partial t} = \lambda_h - \gamma_{nr} n_h - \Gamma N_e N_h - \left.\frac{N_h}{\partial t}\right|_{c-c} - (iV_{cv}\rho_{vc} - iV_{cv}^*\rho_{cv}) \tag{14}$$

where $N_e(k) =< a_k^\dagger a_k >$ is the probability of having electrons with wave vector k, $N_h(k) =< b_{-k}^\dagger b_{-k} >$ is the probability of having holes with wave vector k, $\rho_{cv} =< a_k b_{-k} >$ is the polarization of the momentum state k, and $\rho_{vc} = \rho_{cv}^* =< b_{-k}^\dagger a_k^\dagger >$. In Eqs. 12 through 14

$$V_{cv} = -\frac{\mathbf{d}\cdot\mathbf{E}(\mathbf{r},t)}{2\hbar},$$

where $\mathbf{d}$ is the dipole matrix element between a conduction state and a valence-state (generally k-dependent), $\mathbf{E}(\mathbf{r},t)$ is the electric field, and Γ is the radiative recombination rate constant. In our analysis we use an average value for $\mathbf{d}$, which is assumed to be real. This average value of $\mathbf{d}$ will yield an average value for V_{cv}, which we denote by V_{cv}. Since we assume $\mathbf{E}(\mathbf{r},t)$ to be real, V_{cv} will also be real.

We define

$$n_e(t) = V^{-1}\sum_k N_e$$

as the conduction band electron density,

$$n_h(t) = V^{-1}\sum_k N_h$$

as the the valence band hole density,

$$\mathbf{P}(\mathbf{r},t) = \mathbf{P}_c + \mathbf{P}_c^*$$

as the polarization density, and

$$\mathbf{P}_c = V^{-1}\sum_k \mathbf{d}\rho_{cv}.$$

Since we assumed $\mathbf{d}$ to be independent of k, $\mathbf{P}_c$ can be rewritten as

$$\mathbf{P}_c = \mathbf{d}V^{-1}\sum_k \rho_{cv},$$

where $\mathbf{d}$ now refers to the average dipole moment between the valence and conduction states.

THODE

By summing over k and assuming that ω, γ, and d can be approximately treated as k-independent quantities, Eqs 12 through 14 become, after solving formally for $\sum_k \rho_{cv}$,

$$\frac{\partial n_e}{\partial t} = \Lambda_e - \gamma_{nr} n_e - \frac{\Gamma}{V} \sum_k N_e N_h$$
$$-2V_{cv} \int_0^t V_{cv}(\mathbf{r}, t')[n_e(t') + n_h(t') - n_e^0] e^{-\gamma(t-t')} \cos\omega(t-t')dt' \tag{15}$$

$$\frac{\partial n_h}{\partial t} = \Lambda_h - \gamma_{nr} n_h - \frac{\Gamma}{V} \sum_k N_e N_h$$
$$-2V_{cv} \int_0^t V_{cv}(\mathbf{r}, t')[n_e(t') + n_h(t') - n_e^0] e^{-\gamma(t-t')} \cos\omega(t-t')dt'. \tag{16}$$

We introduce the equation

$$R(\mathbf{r}, t) = 2 \int_0^t V_{cv}(\mathbf{r}, t')[n_e(t') + n_h(t') - n_e^0] e^{-\gamma(t-t')} \cos\omega(t-t')dt' \tag{17}$$

and neglect the spontaneous recombination rate term. Then, Eqs. 15 and 16 reduce to

$$\frac{\partial n_e}{\partial t} = \Lambda_e - \gamma_{nr} n_e - V_{cv} R \tag{18}$$

and

$$\frac{\partial n_h}{\partial t} = \Lambda_h - \gamma_{nr} n_h - V_{cv} R. \tag{19}$$

The final equation required for the gain model is the polarization density in terms of the electric field:

$$\mathbf{P}(\mathbf{r}, t) = 2\mathrm{d} \int_0^t V_{cv}(\mathbf{r}, t')[n_e(t') + n_h(t') - n_e^0] e^{-\gamma(t-t')} \sin\omega(t-t')dt', \tag{20}$$

where n_e^0 is the constant electron density in the conduction plus valence bands at equilibrium.

Equations 17 through 20 constitute the gain medium model. As with the fields, it is convenient to express these equations in terms of dimensionless variables. For the numerical solution, the integral equations 17 and 20 are converted into two coupled differential equations and advanced along with the displacement vector.

4. CARRIER TRANSPORT MODEL

The carrier transport can be described by a set of macroscopic device equations that is commonly referred to as the dual model. In the case of a laser structure, carrier transport in a heterogeneous material system presents new challenges in modeling of coupled electrical and thermal contributions; as well as the additional driving forces caused by composition-dependent band parameters, such as the bandgap, effective mass, and electron affinity. Moreover, the effects of carrier degeneracy and varying lattice/carrier temperature, effects that play an important role in III-V materials, must be included.

The complete set of macroscopic device equations, called the dual energy transport (DUET) model, has been implemented in Stanford's PISCES-2ET code.[14,15,16] The transport model is based on the moment approach to solving the Boltzmann transport equation. The DUET model solves for six independent variables: the electric potential ψ; the electron and hole densities n_e and n_h; the electron and hole temperatures T_e and T_h; and the lattice temperature T_L. These six variables uniquely determine the state of the device since the electron and hole current densities, $\mathbf{j}_e$ and $\mathbf{j}_h$, are determined by the electric potential, electron density, and hole density.

THODE

The equations to be solved are the Poisson's equation, continuity equations for electrons and holes, energy balance equations for electrons and holes, and the thermal diffusion equation for lattice:

$$
\begin{aligned}
-\nabla\cdot\varepsilon\nabla\psi &= q(n_e - n_h + N_D^+ - N_A^-) \\
\frac{\partial n_e}{\partial t} &= \frac{1}{q}\nabla\cdot\mathbf{j}_e - (U_{nr} - R_{sp} - R_{st}) \\
\frac{\partial n_h}{\partial t} &= -\frac{1}{q}\nabla\cdot\mathbf{j}_h - (U_{nr} - R_{sp} - R_{st}) \\
\frac{\partial \omega_e}{\partial t} &= -\nabla\cdot\mathbf{S}_e + \mathbf{j}_e\cdot\mathbf{F}_e - (u_{SRH} + u_{rad})\gamma(\eta_e)\frac{3}{2}k_B T_e \\
&+ (u_{e,auger} - g_{e,imp})[E_g(T_L) + \gamma(\eta_h)\frac{3}{2}k_B T_h] \\
&+ g_{h,imp}\gamma(\eta_e)\frac{3}{2}k_B T_e - \frac{\omega_e - \omega_e^0(T_L)}{\tau_{\omega e}} \\
\frac{\partial \omega_h}{\partial t} &= -\nabla\cdot\mathbf{S}_h + \mathbf{j}_h\cdot\mathbf{F}_h - (u_{SRH} + u_{rad})\gamma(\eta_h)\frac{3}{2}k_B T_h \\
&+ (u_{h,auger} - g_{h,imp})[E_g(T_L) + \gamma(\eta_e)\frac{3}{2}k_B T_e] \\
&+ g_{e,imp}\gamma(\eta_h)\frac{3}{2}k_B T_h - \frac{\omega_h - \omega_h^0(T_L)}{\tau_{\omega h}} \\
C_L\cdot\frac{\partial T_L}{\partial t} &= \nabla(\kappa\nabla T_L) + u_{SRH}[\gamma(\eta_e)\frac{3}{2}k_B T_e + E_g(T_L) + \gamma(\eta_h)\frac{3}{2}k_B T_h] \\
&+ \frac{\omega_e - \omega_e^0(T_L)}{\tau_{\omega e}} + \frac{\omega_h - \omega_h^0(T_L)}{\tau_{\omega h}}
\end{aligned}
$$

In the continuity equations U_{nr} is the net recombination rate due to nonradiative processes; U_{sp} and U_{st} are the spontaneous and stimulated emission rates, respectively. In the energy balance equations $\mathbf{S}_e$ and $\mathbf{S}_h$ denote electron and hole energy flux densities; ω_e and ω_h are the average energies for the electron and hole systems; ω_e^0 and ω_h^0 are the average energies for the electron and hole systems at equilibrium specified by T_L; and $\tau_{\omega e}$ and $\tau_{\omega h}$ are the energy relaxation times for electrons and holes, respectively. In addition, η_e and η_h are quantities related to the Fermi-energy where γ is the Fermi-dirac degeneracy factor.

As can be seen from the equations, the energy is exchanged between carrier subsystems via Auger recombination, $u_{e,auger}$ and $u_{h,auger}$, and impact ionization, $g_{e,imp}$ and $g_{h,imp}$, while the energy exchange among carrier and lattice subsystems is by way of Schockley-Read-Hall (SRH) and phonon scattering. In the simulation of laser diodes, the hot-carrier effect is often not a major concern, and the assumption $T_e = T_h = T_L$ is valid. In that case, a thermodynamic model can be derived from DUET to treat effects due to lattice heating and thermal diffusion.

Currently, the heterostructure modeling capability of PISCES-2ET covers the four main material systems: $Al_xGa_{1-x}As$, $Al_xIn_{1-x}As$, $Ga_xIn_{1-x}As_yP_{1-y}$, and Ge_xSi_{1-x}. These compounds correspond to the base materials of GaAs, InAs, InP, and Si, respectively. The material parameters used in PISCES-2ET have been taken from published values in the literature or from experimental data obtained at the Hewlett-Packard Company.

5. INTEGRATION OF FIELD AND GAIN MEDIUM MODELS

At the present time only the integation of the field and gain models has been completed. With respect to numerical instability, however, the integration of the field and gain models is the critical step in the development of the complete laser model, since the field and gain models are very tightly coupled, whereas the carrier transport occurs on a longer time-scale.

The general vector solution for the integrated field-gain model is complicated and requires the inversion of a large, but sparse, matrix within each quantum well region. This matrix inversion is done by iteration. Unlike the transverse magnetic (TM) and transverse electric (TE) approximations, the full-vector algorithm has not been extensively tested. As a result, we only discuss the TM and TE approximations in two spatial dimensions. For the three-dimensional case the coupled field-gain model is applied to each azimuthal mode.

THODE

5.1. TM approximation

The three field components considered are the longitudinal electric displacement, D_1; the transverse electric displacement, D_2; and the transverse magnetic field, B_3. To increase the computational efficiency of the TM algorithm, we neglect the direct coupling between the quantum well regions and the longitudinal electric displacement. From an energy balance standpoint, the small asymmetry associated with the longitudinal electric displacement can be taken into account by increasing the magnitude of the dipole matrix:

$$d \rightarrow d(1+ < D_1 > / < D_2 >),$$

where $< D_1 >$ is the average longitudinal electric displacement and $< D_2 >$ is the average transverse electric displacement. Except for the neglect of the direct coupling, the longitudinal electric displacement is calculated in a self-consistent manner.

In the TM approximation, the Rabi frequency reduces to

$$\frac{\mathbf{d}\cdot\mathbf{D}}{2\hbar} = \frac{dD_2}{2\hbar}.$$

The electric displacement and the magnetic field are advanced using a leap-frog approach outside the quantum well regions, with the electric displacement advanced on integer time steps and the magnetic field advanced on half-integer time steps. Within the quantum well regions, D_2, R, and P are advanced simultaneously using equations 7, 17, and 20. This step requires a 3x3 matrix inversion at integer time steps. Although the matrix inversion is expensive relative to the advancement of the electric displacement, the inversion is required to maintain numerical stability in the presence of the high-Q cavity. On half-integer time steps, B_3, n_e, and n_h are advanced using equations 1, 18, and 19. This step is straightforward since D_2, R, and P are correctly centered in time.

5.2. TE approximation

The three field components considered are the longitudinal magnetic field, B_1; the transverse electric displacement, D_3; and the transverse magnetic field, B_2. In this approximation, the Rabi frequency reduces to

$$\frac{\mathbf{d}\cdot\mathbf{D}}{2\hbar} = \frac{dD_3}{2\hbar}.$$

With the exception that the D_3 is located at a different position on the mesh than D_2, the rest of the algorithm is identical to the TM approximation.

6. INITIAL TESTING AND RESULTS

With any new or highly modified code, like ours, there is the distinct possibility of either a logic or an accidental error being incorporated into the implementation of the algorithms. This possibility is especially true of a code that is very general: a time-dependent code capable of handling a very complex geometry with multiple materials. As such, the field-gain model has been extensively tested against a number of problems that have analytic solutions: 1) dispersion and damping in coaxial transmission lines; 2) MLD mirror reflection coefficient, transmission coefficient, and bandwidth; 3) coupled quantum well and pill-box cavity resonators, including scaling studies of saturated power with the number of quantum wells; and 4) full-scale VCSEL simulation to investigate transverse modes. We only discuss the MLD mirror and the full-scale VCSEL simulations. Except for the full-scale VCSEL simulation, these test problems are only indirectly related to the laser problem. In other words, a test problem may only address a part of the entire algorithm. Despite this, the testing gives insight into the limits of the algorithms, insight that will be required to understand the validity of a full-scale laser simulation.

6.1. Multilayer dielectric problem

The MLD mirror is the most difficult region of the laser to handle. Since there are often two different MLD mirrors in a VCSEL, the wavelength within the device can change significantly over just a few wavelengths. As a result, the slow amplitude and phase approximations are not valid. Moreover, bulk absorption depends, at the very least, on the radial coordinate. In the most general case, absorption may depend upon the azimuthal coordinate

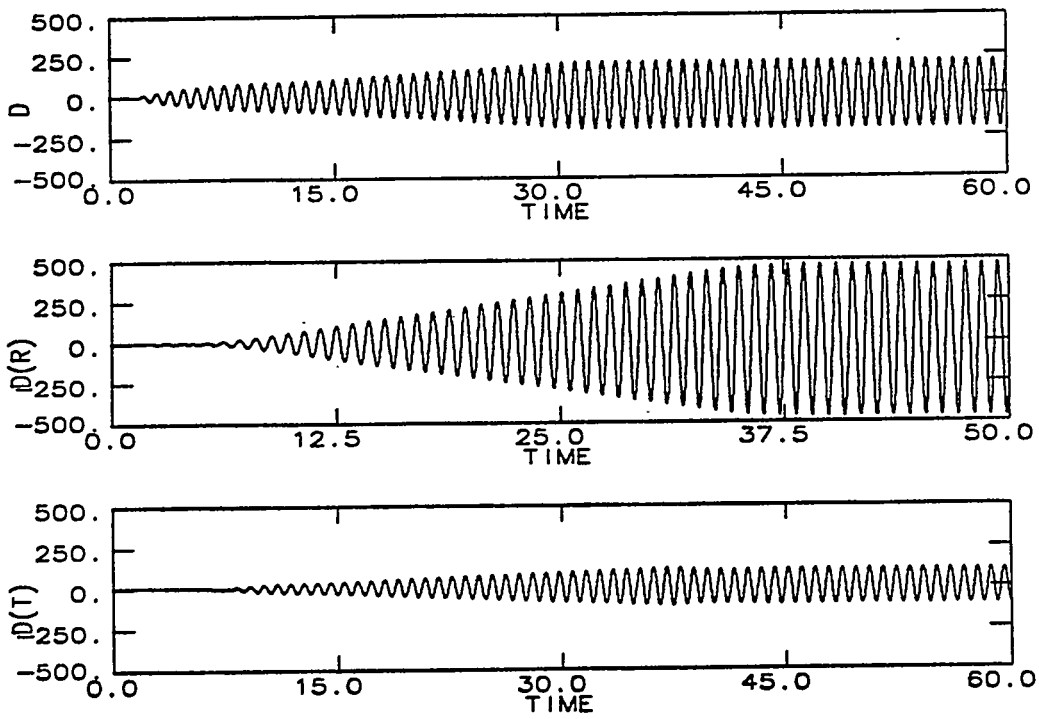

Figure 1: Total electric field (a), reflected electric field (b), and transmitted electric field (c) as a function of time.

as well. As a result, the computational effort required to obtain an accurate three-dimensional solution of the field equations in the MLD mirror region is nontrivial. In the long-term, we plan to replace our present calculation in the MLD region with a reduced model, but we will retain the general capability to calculate the fields in the MLD mirror region as a benchmark for the reduced model calculations.

The solution for the reflection and transmission coefficients for a transverse electromagnetic (TEM) wave incident on a lossless MLD mirror can be calculated from a matrix equation. By varying the frequency of the incident wave, a number of calculations can be performed to obtain the bandwidth of the MLD mirror. Given this, a relevant and difficult test problem is to calculate the bandwidth of an MLD mirror.

A valid approximation for a TEM wave incident onto an MLD mirror is a wave on a coaxial transmission line with an MLD mirror located along the line. For this particular test problem there are 15 dielectric pairs, with an index of refraction for each pair being 1.5 and 1.8, respectively. Vacuum exists on either side of the MLD mirror.

The time dependence of the electric field is shown Fig. 1. As shown, the electric field and time are in dimensionless units. The incident wave was injected with a risetime of 30 ω_p^{-1} to a final amplitude of 477. Fig. 1(a) is the total electric field, which is the sum of the incident and reflected wave, at a position before the MLD mirror; Fig. 1(b) is the reflected wave at the same position before the MLD mirror; and Fig. 1(c) is the transmitted wave at a position after the MLD mirror, but at the same radial position. Above time 30 ω_p^{-1}, the transmission and reflection coefficients have reached steady state.

The transmission coefficient is straightforward to calculate since there is no interference with the incident wave; one simply measures the amplitude of the transmitted wave and divides it by the amplitude of the incident wave, which is known. Since the sum of the reflectance and transmittance is unity, one can determine the reflection coefficient once the transmission coefficient is known. However, this is not the correct way to determine the reflection coefficient, since it assumes conservation of energy. We calculate the transmission and reflection coefficients independently and use that information to determine the level of energy conservation being maintained within the simulation.

The reflection coefficient is more difficult to calculate because the incident and reflected waves combine to form the measured electric field shown in Fig. 1(a). To calculate the reflection coefficient, it is necessary to perform a reference simulation with no MLD mirror present. The electric field from the reference simulation is then subtracted from the MLD mirror simulation to determine the reflected electric field amplitude. This post-processing capability is provided by the code PEG.

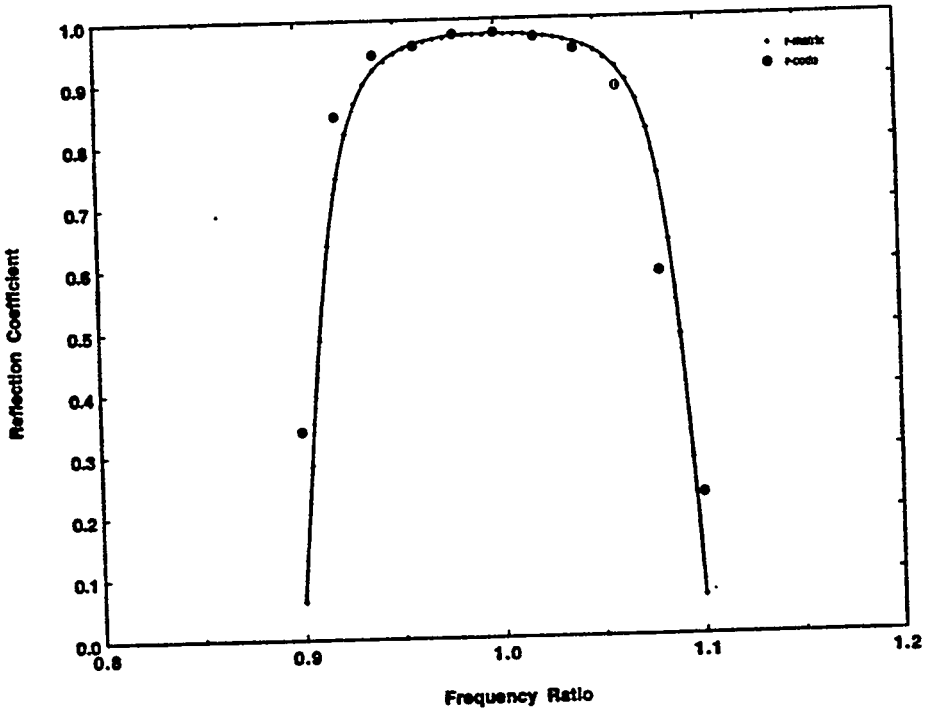

Figure 2: Reflection coefficient as a function of the ratio of incident-to-design frequency.

For this particular case, the reflection coefficient is shown as a function of the ratio of incident-to-design frequency Fig. 2. When all the dielectric layers are one-quarter of a wavelength in thickness at the design frequency, reflection coefficient is symmetric about the design frequency. From the figure, the agreement between the ... equation and the simulation is within 1% around the design frequency. On the other hand, note that the ...tion results are not symmetric about the design frequency. This slight asymmetry is due to the finite difference ...eximation. In this simulation the computational grid is uniform in real space, not wavenumber space. As a result, the dielectric layer thickness differs slightly from the desired one-quarter of a wavelength. The lower index of refraction layer is slightly thicker while the higher index of refraction layer is slightly thinner. This difference leads to the observed asymmetry in the reflection coefficient as well as in the transmission coefficient.

6.2. Full-scale VCSEL problem

The two-dimensional geometry for a full-scale VCSEL simulation is shown in Fig. 3. The dimensions are in microns. In this case, there are 83 different layers made up of 7 different materials. The design is for $\lambda = 0.98\mu m$ operation.

Starting from the left-hand boundary, there is a 51-layer MLD mirror region, a cladding layer, three quantum well layers separated by four barrier layers, another cladding layer, a contact layer, and a 14-layer MLD mirror region. The large annular layer is a metal contact. The quantum wells and associated barriers are split into active and inactive layers, with the active layers limited to about one-half of the inner radius of the metal contact. The metric used for this calculation is cylindrical coordinates with azimuthal symmetry. Although the longitudinal and radial mesh sizes differ, both are uniform in space along either the longitudinal or radial direction. Because this calculation uses a uniform metric, it is necessary to slightly modify the index of refraction of some of the materials by a few percent. In addition, the radial dimension of the simulation is much smaller than in an actual device, the simulation being limited to regions where the electric displacement is large. Except for these two assumptions, the simulation geomerty is a good representation of an actual device.

This simulation is still a test problem for the field-gain model, since the bulk index of refraction is constant within each region. In general, the index of refraction will, at least, depend upon the lattice temperature and carrier concentration for each material. Also, there are regions that exhibit nonuniform absorption. Rather than being calculated from a carrier transport model, the radial and time profiles of the injection currents are specified

THODE

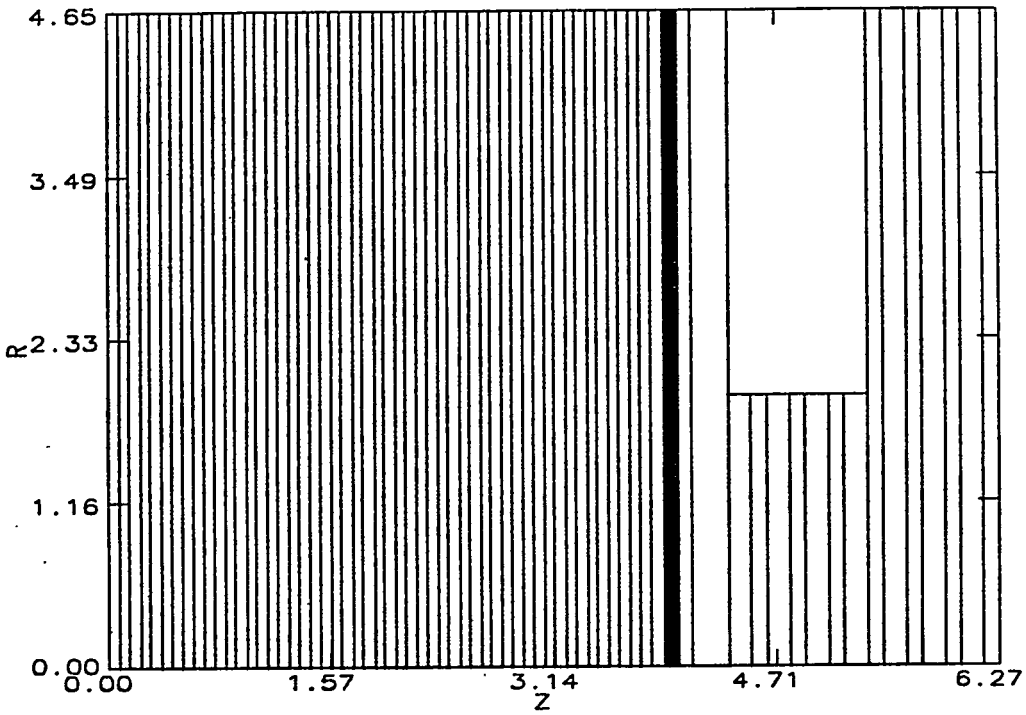

Figure 3: Geometry for a full-scale VCSEL simulation.

functions. Finally, the field-gain model is limited to the TM approximation, not the full-vector solution.

The transverse electric displacement field is shown as a function of the longitudinal coordinate in Fig. 4. The location of this slice is near the axis of the laser. As expected, there is a well-defined standing-wave pattern indicating the presence of a single longitudinal mode. At the left-hand boundary a perfect-metal boundary condition is specified. The wavelength varies significantly throughout the laser as the index of refraction varies over just a few wavelengths. The power is outcoupled through the right-hand boundary assuming a phase velocity that is characteristic of the last material layer.

The time-averaged Poynting vector through the right-hand boundary is shown at various times in Fig. 5. The Poynting vector is normalized to the total power to bring out the profile which, after going through some transient behavior, settles down to a well-defined pattern. Note that this is not a single transverse mode but the total field pattern. We have not made any assumptions about the transverse mode content of the field other than the TM approximation. If desired, this transverse pattern can be decomposed into a set of transverse modes. In this case, the pattern consists of two intense annular rings with the outer ring being more intense than the inner ring. In addition there is a faint halo outside of the two intense rings.

7. SUMMARY

Our QWL code development effort is part of a Cooperative Research and Development Agreement (CRADA) between the Los Alamos National Laboratory and the Hewlett-Packard Company. The experimental results obtained by the Hewlett-Packard Company indicate that a VCSEL must be described by a three-dimensional model. A simulation code to accurately describe the operation of a VCSEL must integrate a tightly coupled set of field, gain medium, and carrier transport equations. First, the field-gain model must solve for a frequency dependent gain in the time domain, with a temperature dependent bandgap. In other words, the model must allow the frequency to chirp. Second, the tansverse mode separation must be calculated in three dimensions, the accurate calculation of MLD mirrors must be possible, and the coupling between transverse magnetic and transverse electric modes must be taken into account. Third, the transport model must include energy transport in heterostructures and lattice temperature evolution. Finally, the geometry is complex, with spatially dependent absorption, gain, and dispersion.

THODE

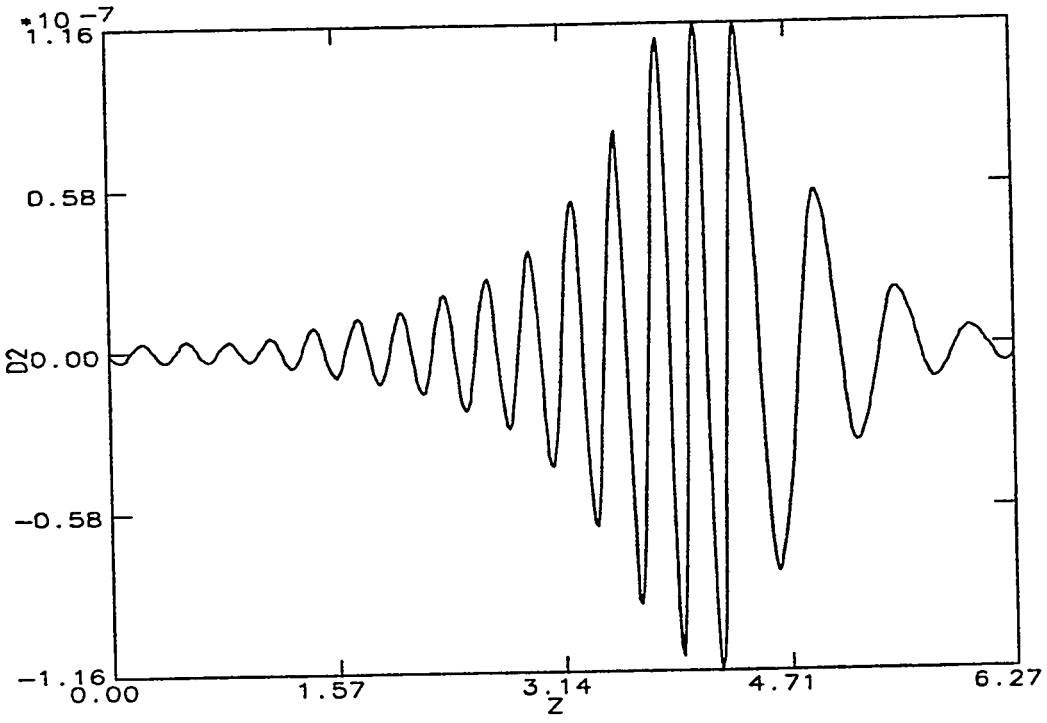

Figure 4: Standing wave pattern of the transverse electric displacement close to the axis of the laser.

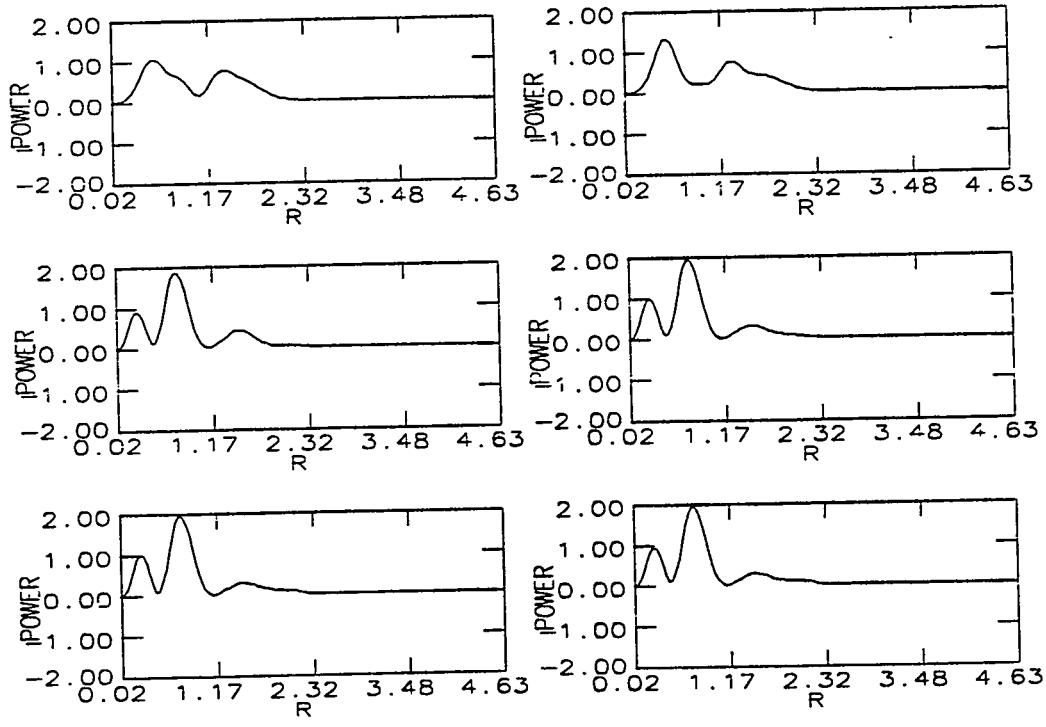

Figure 5: Time-averaged Poynting vector profile at different times.

The bulk index of refraction and absorption are frequency independent but can evolve slowly in time due to lattice temperature variation.

A numerically stable field-gain model has been developed that is second-order accurate both in space and time. The field-gain model has been extensively tested against a number of problems that have analytic solutions: 1) dispersion and damping in coaxial transmission lines; 2) MLD mirror reflection coefficient, transmission coefficient, and bandwidth; 3) coupled quantum well and pill-box cavity resonators, including scaling studies of saturated power with the number of quantum wells; and 4) full-scale VCSEL simulation to investigate transverse modes.

The two-dimensional model is extended to a three-dimensional model by assuming that the spatial dependence in the azimuthal direction is periodic. With this assumption, the two-dimensional coupled field-gain model is then applied to each azimuthal mode. This field-gain model will be integrated with a carrier transport model to form the self-consistent laser code, VCSEL.

8. ACKNOWLEDGMENTS

The Los Alamos National Laboratory portion of the CRADA is supported by the U. S. Department of Energy. We gratefully acknowledge Charles Snell for the update utility for the HP 735 workstation, Jim Morel for the matrix inversion algorithm used in the TM and TE approximations , Mike Tan for many enlightening disscusions concerning the experimental results, and Chris Fontes for providing us with an number of LaTEX macros for the SPIE format. One of us (LET) gratefully acknowledges David Cartwright for his efforts in starting and maintaining an interest in the CRADA with the Hewlett-Packard Company.

9. REFERENCES

[1] K.Y. Lau, N. Bar-Chaim, I. Ury, Ch. Harder, and A. Yariv, *Appl. Phys. Lett.* **43**, 1 (1983).

[2] Y. Arakawa and A. Yariv, *IEEE J. Quantum Electron.* **QE-21**, 1666 (1985).

[3] Y. Arakawa and A. Yariv, *IEEE J. Quantum Electron.* **QE-22**, 1887 (1986).

[4] Y. Arakawa, K. Vahala, A. Yariv, and K. Lau, *Appl. Phys. Lett.* **48**, 384 (1986).

[5] I. Suemune, L.A. Coldren, M. Yamanishi, and Y. Kan, *Appl. Phys. Lett.* **53**, 2378 (1988).

[6] K.Y. Lau, "Dynamics of Quantum Well Lasers" in **Quantum Well Lasers** (Ed. P. Zory, Academic, 1983) p.217.

[7] K. S. Yee, *IEEE Trans. Ant. Prop.* **AP-14**, 302 (1966).

[8] M. M. Campbell, B. B. Godfrey, and D. J. Sullivan, " IVORY User's Manual", *Mission Research Corporation report AMRC-R-4554* (October 1988).

[9] H. Haug, "Microscopic Theory of the Optical Band Edge Nonlinearities, " in **Optical Nonlinearities and Instabilities in Semiconductors**, edited by H. Haug (Academic, New York, 1988) p.53.

[10] J. Schwinger,*J. Math. Phys.* **2**, 407 (1961).

[11] L.V. Keldysh, *Sov. Phys. JETP* **20**, 1018 (1965).

[12] M. Lindberg and S.W. Koch, *Phys. Rev. B* **38**, 3342 (1988).

[13] M. Sargent III, F. Zhou, and S.W. Koch, *Phys. Rev. A* **38**, 4673 (1988).

[14] M. R. Pinto, C. S. Rafferty, and R. W. Dutton, " PISCES-II User's Manual," Stanford University, CA, 1984.

[15] D. Chen, E. C. Kan, U. Ravaioli, C.W. Shu and R. W. Dutton, *IEEE Elec. Dev. Lett.* **13**, 26 (1992).

[16] D. Chen, E. Sangiorgi, M. R. Pinto, E. C. Kan, U. Ravaioli and R. Dutton, "Analysis of spurious velocity overshoot in hydrodynamic simulations of ballistic diodes, " *Proceeding of NUPAD V (Numerical Process and Device Modeling Workshop)*, Seattle, May 31 – June 1, 1992.

THODE